Characterizing reflectance anisotropy of background soil in open-canopy plantations using UAV-based multiangular images

Linyuan Li [a,b,c], Xihan Mu [a,*], Jianbo Qi [b], Jan Pisek [d], Peter Roosjen [e], Guangjian Yan [a], Huaguo Huang [b], Shouyang Liu [c], Frédéric Baret [c]

[a] *State Key Laboratory of Remote Sensing Science, Faculty of Geographical Science, Beijing Normal University, 100875 Beijing, China*
[b] *Key Laboratory for Silviculture and Conservation of Ministry of Education, Beijing Forestry University, 100083 Beijing, China*
[c] *INRAE EMMAH UMR1114, Domaine Saint-Paul, Site Agroparc, 84914 Avignon Cedex 9, France*
[d] *Tartu Observatory, University of Tartu, Observatooriumi 1, Tõravere 61602, Tartumaa, Estonia*
[e] *Laboratory of Geo-Information Science and Remote Sensing, Wageningen University & Research, Droevendaalsesteeg 3, 6708 PB Wageningen, Netherlands*

ARTICLE INFO

ABSTRACT

The canopy bidirectional reflectance distribution function (BRDF) plays a pivotal role in estimating the biophysical parameters of plants, whereas soil background anisotropy creates challenges for their retrieval. Soil optical properties affect canopy anisotropic characteristics, especially in open-canopy areas. However, the remote sensing of background anisotropy is challenging due to the difficulties of information extraction in complex forest ecosystems and varying illumination conditions. This study develops an efficient photogrammetric technique to extract the background soil bidirectional reflectance factor (BRF) from unmanned aerial vehicle (UAV)-based multiangular images and to verify the need for accurate soil anisotropy information in canopy radiative transfer modeling. Soil BRF profiles were measured over three open-canopy sample plots from multiangular remotely sensed multispectral images collected with a hexacopter. As validation, reference soil BRF profiles were synchronously acquired by a ground-based multiangular imaging system.

A high level of consistency between the ground- and UAV-measured soil BRF was observed with an RMSE of less than 0.012. Uncertainty analysis of the measured soil BRF showed that multiple scattering between sunlit soil in large sunflecks and foliage elements contributed less than 5%. Both results demonstrated that soil anisotropy can be accurately extracted from UAV multiangular measurements. To explicitly demonstrate that the use of soil anisotropy can reduce uncertainties in canopy radiative transfer simulations, we simulated the canopy BRF with Lambertian soil and with anisotropic soil using a three-dimensional (3D) radiative transfer model under different soil moisture content (SMC) levels, canopy cover (CC) levels and solar zenith angles (SZAs) with simulated realistic forest scenes. We found that less CC, lower SZAs and less SMC lead to a more significant influence of soil anisotropy on canopy reflectance; e.g., the reflectance bias reaches up to 0.3 in the hotspot direction. This illustrates that neglecting soil anisotropy can cause considerable errors in the modeling of the canopy BRF of open forests (i.e., CC levels of less than 0.5). The proposed technique facilitates the characterization of anisotropic forest background soil, which is important for advancing canopy radiative transfer modeling and validation and for the retrieval of vegetation parameters.

1. Introduction

Surface reflectance anisotropy, typically described by the bidirectional reflectance distribution function (BRDF), is an inherent characteristic of land surfaces. The measure depends on surface three-dimensional (3D) structures, optical properties, and the sun-sensor geometry. Due to the extreme difficulty of BRDF measurement in the field, an alternative term, bidirectional reflectance factor (BRF) has been proposed to characterize the reflectance anisotropy. Many semi-empirical and physically-based canopy BRDF models have been developed over the past decades (e.g., Huang et al., 2009; Kuusk, 2001; Kuusk and Nilson, 2000; Roujean, 1992; Verhoef, 1984). The retrieval of canopy biophysical and biochemical variables can be achieved by inverting these models when directional reflectance measurements are available (Combal et al., 2003; Gao et al., 2003; Laurent et al., 2011; Mu et al., 2018; Weiss and Baret, 1999; Yan et al., 2016; Baret and Buis, 2008).

It is noteworthy that vegetation canopy anisotropy is a function of the optical and structural properties of both plants and the underlying background. The emphasis of canopy BRDF modeling is typically placed on the relationship to canopy structures and leaf optical properties, whereas background soil properties are given as input based on the simple Lambertian assumption. Generally, the reflectance of Lambertian soil, as the input of the canopy radiative transfer model, is measured from the nadir direction in field measurements. Previous studies have made efforts to find a practical and reliable method of forest background reflectance estimation from satellite reflectance data (Canisius and Chen, 2007; Eriksson et al., 2006; Pisek et al., 2010). However, these earlier attempts simplified soil properties as Lambertian for operational retrievals.

Many studies have reported that soil reflectance is strongly anisotropic (e.g. Cierniewski et al., 2004; Jacquemoud et al., 1992; Liang and Townshend, 1996), and the Lambertian background assumption is insufficient for modeling canopy BRDF (Verhoef and Bach, 2007), especially in semiarid landscapes with sparse vegetation (Ni and Li, 2000). The large gap probability of sparse vegetation canopies leads to a large contribution from soil to canopy BRDF (Kimes, 1991). Therefore, the soil anisotropy considerably affects the anisotropic characteristics of the discrete vegetation canopy (Zarco-Tejada et al., 2001). Pisek et al. (2010) found the retrieved forest background reflectance to be inconsistent with the measured reflectance when the background has strong anisotropic characteristics, demonstrating the importance of background anisotropy of surface variable retrievals. Generally, the intervention of forest background affects the overstory signal, leading to more difficulty with canopy variable retrievals (Canisius and Chen, 2007; Eriksson et al., 2006; Gemmell, 2000).

Studies have considered background soil anisotropic characteristics in the modeling of canopy directional reflectance to improve the accuracy of retrievals (Pinty et al., 1998; Verhoef and Bach, 2007). For example, Schwieder et al. (2020) estimated above-ground biomass and LAI of grassland from Sentinel-2 data with a soil-leaf-canopy (SLC) BRDF model where the soil input was obtained by measuring reference BRF on adjacent pixels of bare soil. However, their soil-canopy BRDF models have rarely been used for practical retrievals due to the challenge of obtaining soil BRF from remote sensing data (Fang and Liang, 2003).

Forest background anisotropy is traditionally measured with a field goniometer and spectrometer (Peltoniemi et al., 2005; Sandmeier and Itten, 1999). However, direct solar illumination is usually not available due to obstruction by trees, especially for large off-nadir angles. An alternative light source is needed in some cases (Peltoniemi et al., 2005). Besides, ground-based observations only focus on a very small area that might not representatively characterize the forest background (Sandmeier and Itten, 1999; Yan et al., 2012). Additionally, most ground-based goniometers are very heavy and require much work to assemble and move (Yan et al., 2012). The abovementioned factors greatly limit forest background measurements in the field.

In several recent studies, unmanned aerial vehicles (UAVs) have been used as platforms for close-range (i.e., in the range of dozens to hundreds of meters) multiangular measurements (Burkart et al., 2015; Kuusk et al., 2014; Schneider-Zapp et al., 2019). UAVs can measure canopy anisotropy with improved angular sampling and high ground sample distance (GSD), i.e., millimeter to centimeter resolution, relative to satellite sensors (Roosjen et al., 2017; Zhang et al., 2020). Roosjen et al. (2018) and Sharma et al. (2013) employed UAV-based canopy BRDF measurements to retrieve the leaf area index (LAI), leaf chlorophyll content, canopy fraction and volume by inverting a physically-based radiative transfer model. However, the authors could ignore the influence of background anisotropy due to the presence of continuous, homogeneous vegetation cover in their target areas. UAV-based multi-angular remote sensing has the potential to access forest background anisotropy from ultrahigh-resolution images over open forest areas and to provide new, much-needed insight into the role and effect of soil anisotropy.

In this study, our objective was to develop a method to obtain the background soil BRF of open-canopy areas using UAV-based multi-angular images. Through a 3D radiative transfer model, named LESS (Large-scale remote sensing data and image simulation framework) (Qi et al., 2019), we explored the uncertainty of the proposed method and the need for accurate soil anisotropy information in canopy radiative transfer modeling. The feasibility and the potential value of the proposed method were discussed.

2. Materials

2.1. Experimental site

Three open orchard plots of approximately 1000–2500 m^2 with planted apricot or peach trees located in Huailai county, North China (40.34°N, 115.78°E) were chosen as test plots for this study (Fig. 1a, Table 1). For selection, flat ground surface, canopy cover level (CC, defined as the proportion of forest floor covered by the vertical projection of the tree crowns where the within-crown gaps are excluded (Korhonen et al., 2006)), and background soil and tree species, and composition homogeneity criteria were applied. The trees were irregularly planted in the plots (Fig. 1b–d). The plantation landscape includes a collection of trees of different ages. The study area has a semi-humid continental climate with elevations ranging from 480 m to 485 m above sea level. The orchard background is composed of bare clay soil occasionally covered with scattered senescent leaves and grasses. It rained two days before the field campaign, and the experiment was conducted in a rainy season window. The soil surfaces beneath the canopy were dry with a soil moisture content of less than 18% (Table 1). The background soil of each plot was spatially homogeneous. The field campaign was conducted in cloud-free and windless atmospheric conditions on 30–31 July 2019.

2.2. Acquisition of UAV data

The DJI M600pro UAV (DJI Technology Co., Ltd. Shenzhen, China) equipped with a GPS, barometer, compass, and inertial measurement unit (IMU) was used to collect remotely sensed images. During the flight, the longitude, latitude, altitude, and yaw of each waypoint were recorded. An active gimbal was installed onto the UAV, controlling the pitch and roll (2D stabilization) of the camera payload to achieve the predetermined view angles. A multispectral camera (MAPIR survey 3 N RGN, manufactured by Peau Productions, Inc., San Diego, USA) mounted on the UAV records three spectral narrow bands with central wavelengths of 550 nm, 660 nm, and 850 nm. The camera integrates an RGN filter in front of the lens and a Sony Exmor IMX117 sensor with a Bayer filter. This assembly causes that the red and green channels were to be mixed with a certain amount of near-infrared (NIR) flux, i.e., only the signal of the NIR band is with high physical fidelity. The camera has
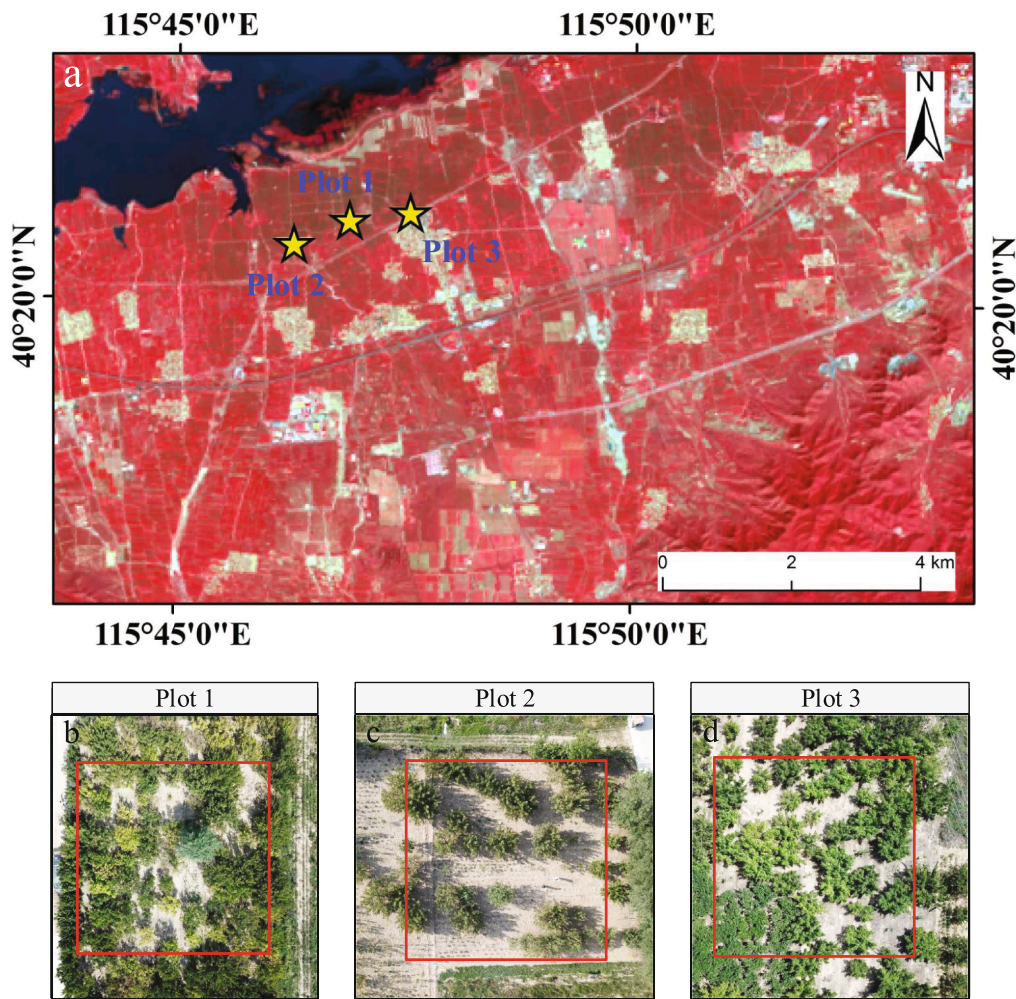
Fig. 1. Study area. (a) Landsat 8 OLI color-infrared image of the experimental site in Huailai County, North China. The yellow stars correspond to the plot positions. (b–d) Perspective views of the three orchard plots with irregularly planted trees are shown by UAV RGB images. The red squares denote the study plot borders. (For interpretation of the references to color in this figure legend, the reader is referred to the web version of this article.)

Table 1
Overview of the three orchard sample plots. Each field measurement is an average of approximately 10 samples.

Sample	Area (m^2)	Plantation						Clay soil
		Species	LAI	Canopy cover	Crown diameter (m)	Tree height (m)	Crown base height (m)	Moisture (%)
Plot 1	30 × 30	Apricot	2.36	0.58	3.38	3.36	0.49	15.35
Plot 2	30 × 30	Apricot	1.71	0.34	3.08	2.91	0.65	9.18
Plot 3	45 × 45	Peach & Apricot	2.83	0.62	2.99	2.57	0.55	17.32

a focal length of 8.25 mm with a field of view (FOV) of 41° × 31° and 4000 × 3000 pixels with the radiometric resolution of 12 bits. The shutter speed of the camera can be manually adapted to adapt the illumination.

The aerial campaigns were performed to collect multiangular images for all the plots. A goniometric flight pattern capturing the plot area as the center of a hemisphere with a radius of 100 m was applied in the campaign (Fig. 2a). We developed a script to predesign waypoints and view angles before each flight. Transects along the principal plane (PP, i. e., a relative azimuth of 0° or 180° with the sun direction)) and along the vertical plane (VP) were applied. The waypoints were defined with an angular step of 5° from −60° (backward scattering direction) to + 60° (forward scattering direction) in each transect. One additional angular observation was performed in the hotspot direction. The UAV

automatically flew along the waypoints at a flight speed of 3 m/s, and the UAV-borne camera was automatically adjusted to continuously point towards the center of the plot. Besides, the UAV also acquired the images of reference panels (Lambertian surfaces with known reflectance) placed on an open space next to the plot before the UAV left the home point and after returned to the home point.

The UAV was launched during two periods with different sun geometries for each plot (Table 2), automatically flying along the predetermined flight route. The multispectral camera had a footprint of 76 × 57 m^2 with a GSD of around 2 cm when the nadir observation was conducted at 100 m above ground level (AGL). The entire UAV mission of multiangular observations was taken during an approximately 10-minute-long flight. Table 2 shows an overview of our UAV-based multiangular observations, accompanying by ground-based measurements.
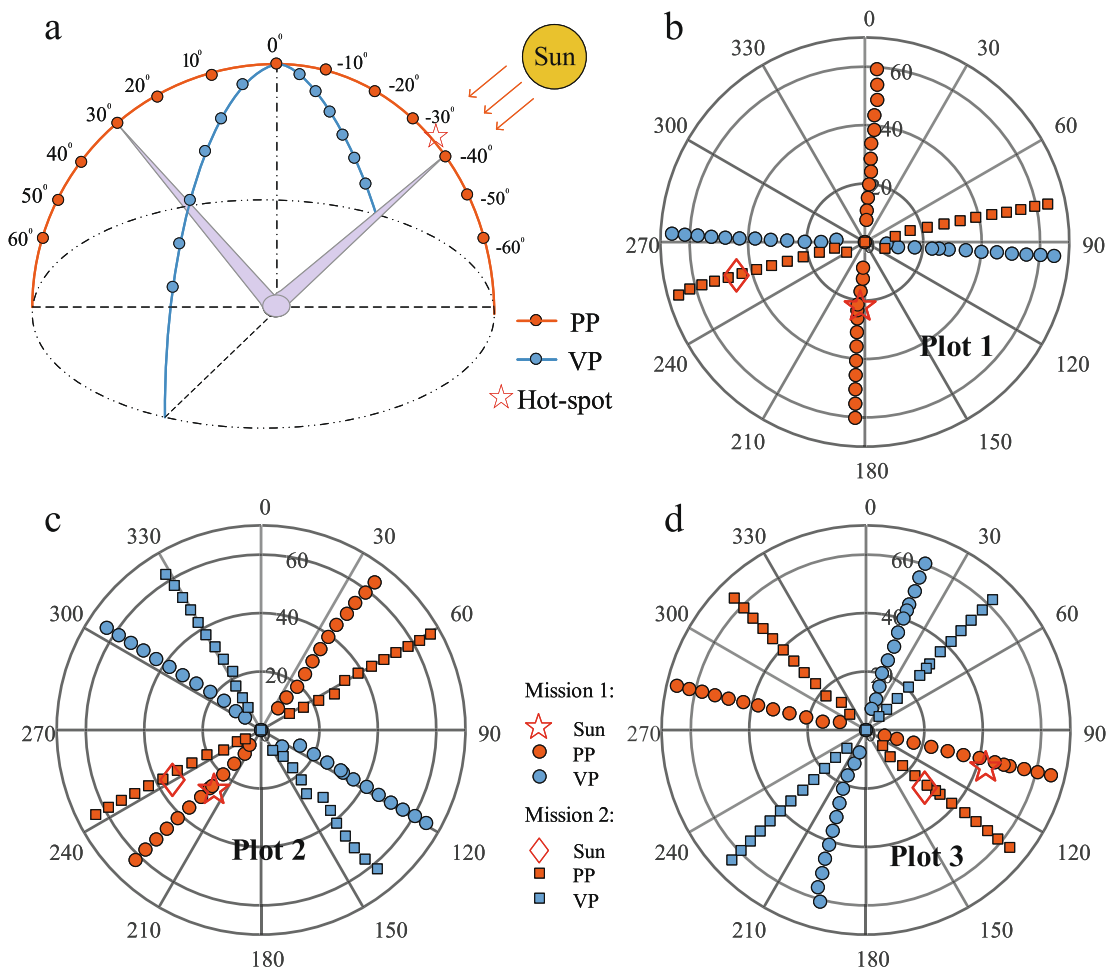
Fig. 2. The flight pattern and actual view geometry. (a) Illustration of the goniometric flight pattern applied in this study, (b–d) Polar plots of the illumination geometry and angular distribution of the view angle during UAV-based multiangular image acquisition (b, c, and d, respectively, for Plots 1, 2, and 3). The orange and blue symbols refer to the averaged view geometry of the target area at the waypoints. The red stars and diamonds correspond to the sun positions during the flight. PP and VP represent the principal and vertical planes, respectively. (For interpretation of the references to color in this figure legend, the reader is referred to the web version of this article.)

Table 2
Overview of the UAV-based and ground-based multiangular measurements taken at three plantation plots. Abbreviations include solar azimuth angle (SAA), solar zenith angle (SZA), view zenith angle (VZA), principal plane (PP), and vertical plane (VP).

Plot	Date	SAA [°]	SZA [°]	UAV-based multiangular measurements					Ground-based multiangular measurements		
				R[1]	Flight time	PP	VP	VZA	Operation time	PP & VP	VZA
Plot 1	30.07.2019	184.21	23.5	100 m	~9 mins	√	√	−60° to +60° (interval of **5**°)	~13 mins	√	−60° to +60° (interval of **5**°)
	31.07.2019	255.47	45.5		~9 mins	√	√		~10 mins	√	
Plot 2	30.07.2019	218.22	30.8		~10 mins	√	√		~10 mins	√	
	30.07.2019	240.66	42.8		~10 mins	√	–		~9 mins	√	
Plot 3	31.07.2019	134.44	33.5		~9 mins	√	√		~10 mins	√	
	30.07.2019	107.34	48.5		~9 mins	√	√		~9 mins	√	

R[1] refers to the flight radius of the goniometer-mode multiangular observation of the UAV, as illustrated by Fig. 2. One additional angular measurement was collected in the hotspot direction for each group of multiangular measurements.

Given that the sun moved less than 3° both in zenith and azimuth during an observation period, for the sake of simplicity, the solar zenith angle (SZA) and solar azimuth angle (SAA) were assumed to be constant for data processing. Finally, each multiangular mission produced 52 images. Fig. 2b–d shows the angular distribution of the average view angle over the plot area of each plot. Note that the UAV images in the VP of Plot 1 were omitted due to an abruptly changed illumination by a small piece of cloud. It is also noticed that the actual flight transects appeared to differ slightly from the nominal ones due to uncertainties in UAV positioning and camera orienting.

2.3. Acquisition of ground data

Ground-based multiangular measurements were taken using a customized portable multiangular observation system illustrated in Fig. 3a, synchronizing with aerial measurements. The system includes a tripod, a pole, a rotatable arm, a pivot, and a multispectral camera (MAPIR survey 3N RGN) consistent with the camera on UAV. The rotatable arm is mounted onto the pole interface and can be adjusted to achieve different zenith angles according to the circular protractor on the pole interface. The system carried on multiangular observations at a
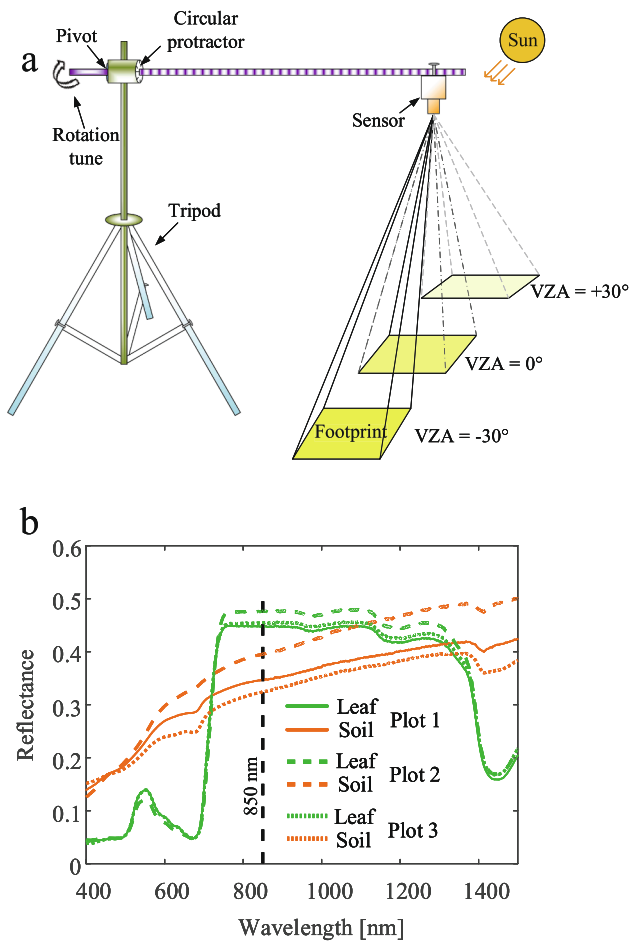
Fig. 3. Overview of the ground-based spectral campaign. (a) Illustration of the ground-based multiangular observation system. (b) Average spectral reflectance of leaves and soil sampled in sample plots.

height of 1.7 m, resulting in a nadir footprint of approximately 1.3 m × 1.0 m. It collected multispectral images with a 10° zenith resolution in the PP and VP over approximately 10 min through manual control. Besides, the ground system acquired the images of the reference panels through manual control before the first image and after the last image acquired in each plane.

The ground-based multiangular images were used to derive the reference BRF profiles of soil as the validation data of UAV-measured soil BRF. The images were firstly radiometrically calibrated as described in Section 2.4. Then the sunlit soil pixels in the central area of each image were visually selected to calculate the soil BRF by averaging the directional reflectance of these pixels. The extracted soil BRF profile was able to represent the soil BRF of the whole plot because the soil physical property and chemical composition are spatially homogeneous in such a cultivated plantation plot.

The ground campaign also involved the measurements of leaves and soil spectral reflectance, soil moisture, and canopy structural parameters (i.e., LAI, crown diameter, tree height, and crown base height). The spectral reflectance of the leaves and soil were collected in the nadir direction using an ASD FieldSpec 3 (Analytical Spectral Devices, Inc., USA). Approximately ten samples were obtained for each class, and an average reflectance was taken after radiometric calibration (Fig. 3b). Soil moisture was sampled from 0 cm to 6 cm in depth using an impedance probe sensor with an HH2 recording device (Delta-T Devices, Cambridge, United Kingdom). In each plot, ten measurement locations were recorded for soil moisture. The LAI was measured using the TRAC optical instrument (3rd Wave Engineering, ON, Canada) along several

30-m transects. Tree heights were collected using a DISTO A5 hypsometer (Leica Geosystems AG, Heerbrugg, Switzerland). The crown diameter was measured by averaging two measurements taken from two measuring tapes laid perpendicular to each other at the largest width of each crown. The crown base height was recorded using a tape measure.

2.4. Radiometric calibration

All UAV-based and ground-based multiangular images were radiometrically calibrated. The radiometric calibration procedure was only conducted for the NIR band because of its physically high fidelity. Firstly, raw images were imported into MAPIR camera control kernel software (MCC) and exported into a 16-bit lossless compression format, i.e., Tagged Image File Format (TIFF), ensuring the compatibility with image processing with common analysis software. Next, the vignetting effect should be theoretically corrected because it can cause a radial reduction in brightness towards the image edges. However, the vignetting effect was neglected as the pixels of the plantation plot were located at the central areas of each image that were marginally influenced by vignetting effect. Finally, the digital number (DN) values of the NIR image were converted to BRF values using a simplified empirical line regression calibration method, since the DN values have a linear relationship to BRF. The linear coefficients can be derived using a MAPIR calibration ground package containing four individual felt-like materials with known reflectance (2%, 21%, 27%, and 83%) served as the Lambertian surfaces (an example shown in Fig. 4). The average DN value (DN_n) of nadir observation from each reference target was extracted from a visually selected region of interest. The coefficients a and b can be obtained by a linear fit (Eq. (1)):

$$BRF_n = a \cdot DN_n + b \tag{1}$$

where BRF_n refers to the nadir BRF of a Lambertian surface while a and b are the slope and intercept, respectively. Given that the linear coefficients are affected by illumination flux, the radiometric calibration was independently executed for each multiangular mission.
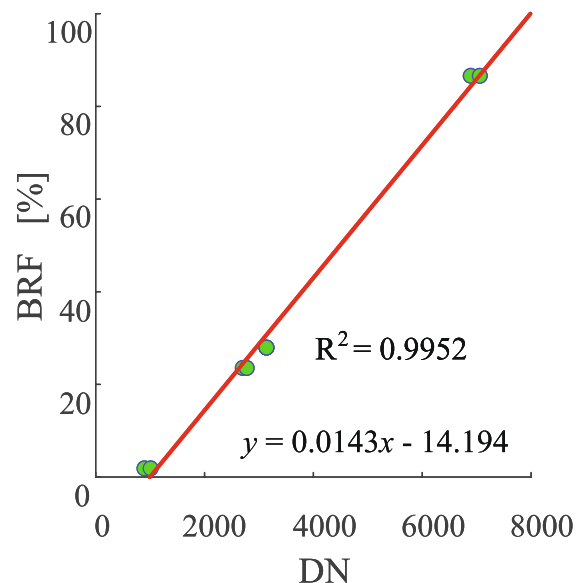

Fig. 4. An example of a linear regression model used to calibrate the digital number (DN) to BRF by four reference panels (Lambertian surfaces with the reflectance of 2%, 21%, 27%, and 83%, respectively). In this example, two images of the reference panels were captured during a multiangular mission, yielding eight data points.

3. Methods

We describe a general synopsis of this study in Fig. 5 including the synchronized observations (UAV-based and ground-based), soil BRF extraction method, BRDF modeling, quantitative analyses, and simulations. UAV- and ground-based multiangular measurements were synchronously collected during a field campaign where the ground-based soil BRF were used to validate the UAV-based soil BRF. The soil BRF extracted from UAV measurements characterized the soil reflectance anisotropy over the whole hemisphere by adjusting a soil BRDF model named SOILSPECT. The modeled soil BRFs were then imported into the LESS model to analyze the uncertainty of UAV-based soil BRF extraction due to multiple scattering. Finally, the influence of soil anisotropy on canopy BRF was quantitatively evaluated by comparing the LESS-simulated canopy BRF under anisotropic and isotropic soil based on extending data from Jacquemoud et al. (1992). The following subsections provide details of the steps in Fig. 5.

3.1. Background soil BRF characterization

3.1.1. Soil BRF extraction from UAV multiangular images

The extraction of soil BRF from UAV-based multiangular images consists of four main steps: (1) 3D point cloud and digital surface model (DSM) are reconstructed from multiangular overlapped images using a photogrammetry technique. The camera positions are also re-estimated during this process; (2) The geolocation of image pixels within the sample plot is calculated based on the collinearity restrictions between DSM and image pixels; (3) The pixel-wise view geometry is calculated using the camera positions and georeferenced pixels; (4) The sunlit soil pixels of plantation background is automatically extracted using the 3D point cloud back-projection and image segmentation. The soil BRF value is derived by aggregating the extracted sunlit soil pixels. These four steps are illustrated in Fig. 6 and are described hereafter.

(1) Reconstruction of 3D point cloud and DSM

The overlapped UAV-based multiangular multispectral images together with the corresponding geographic information of waypoints were imported into Agisoft PhotoScan Professional 1.4.5 (Agisoft LLC, St. Petersburg, Russia) to generate a 3D point cloud of the orchard scenario and a georeferenced DSM (Fig. 6, Waypoints POS, DSM and Sample point cloud). The reconstructed point cloud and DSM were trimmed along the border of each orchard plot. PhotoScan integrates a structure-from-motion algorithm (SfM, also called bundle adjustment in photogrammetry) and a multi-view stereo algorithm (MVS), enabling the identification of identical features within each image, the image match among images, and the re-estimation of the camera positions and orientations based on the waypoint POS and feature matching results. To facilitate feature detection and matching, color-infrared images (layer stacked by red = 850 nm, green = 660 nm, and blue = 550 nm) were processed instead of single-band images. Our processing steps are consistent with the standard PhotoScan processing pipeline, as can be found in the PhotoScan user manual. We used the *high accuracy* and *reference* settings for image alignment to obtain accurate camera positions with a maximum Z error of less than 1 m and maximum X and Y errors of less than 0.5 m. After mesh and DSM building, both the DSM and re-estimated camera information was exported with the WGS84/UTM coordinate system.
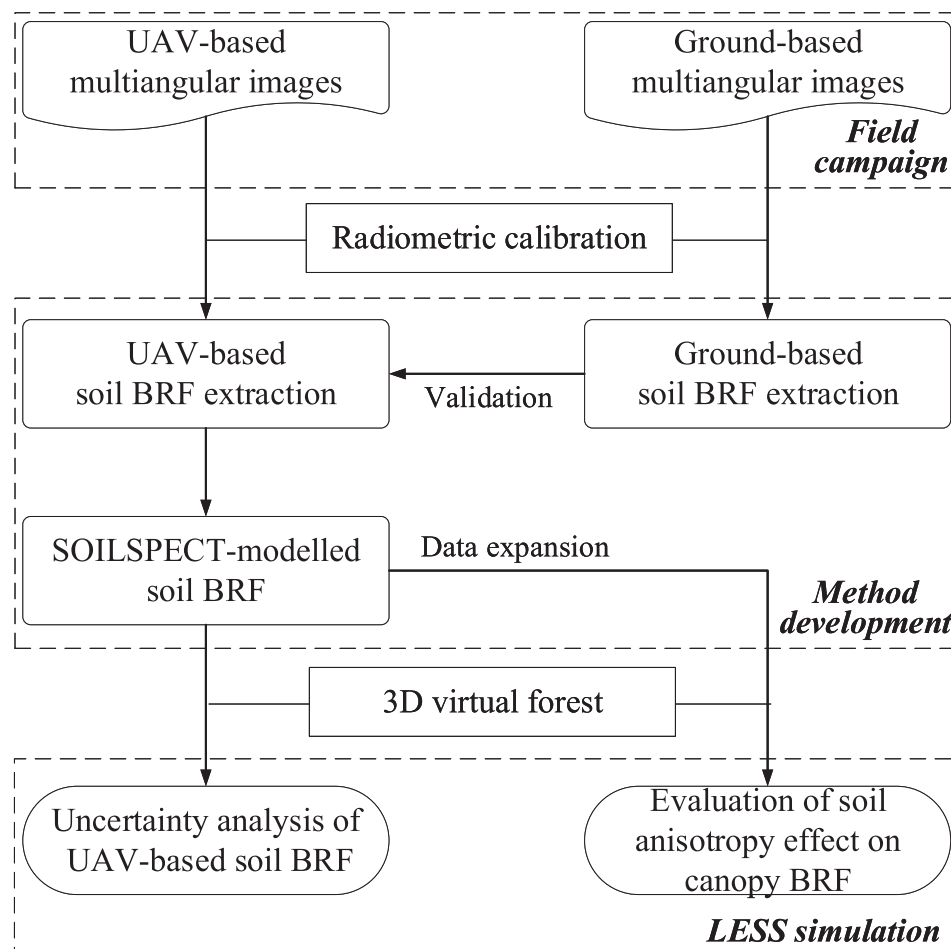

Fig. 5. The analysis framework of this article mainly includes field campaign, method development, and LESS simulation.
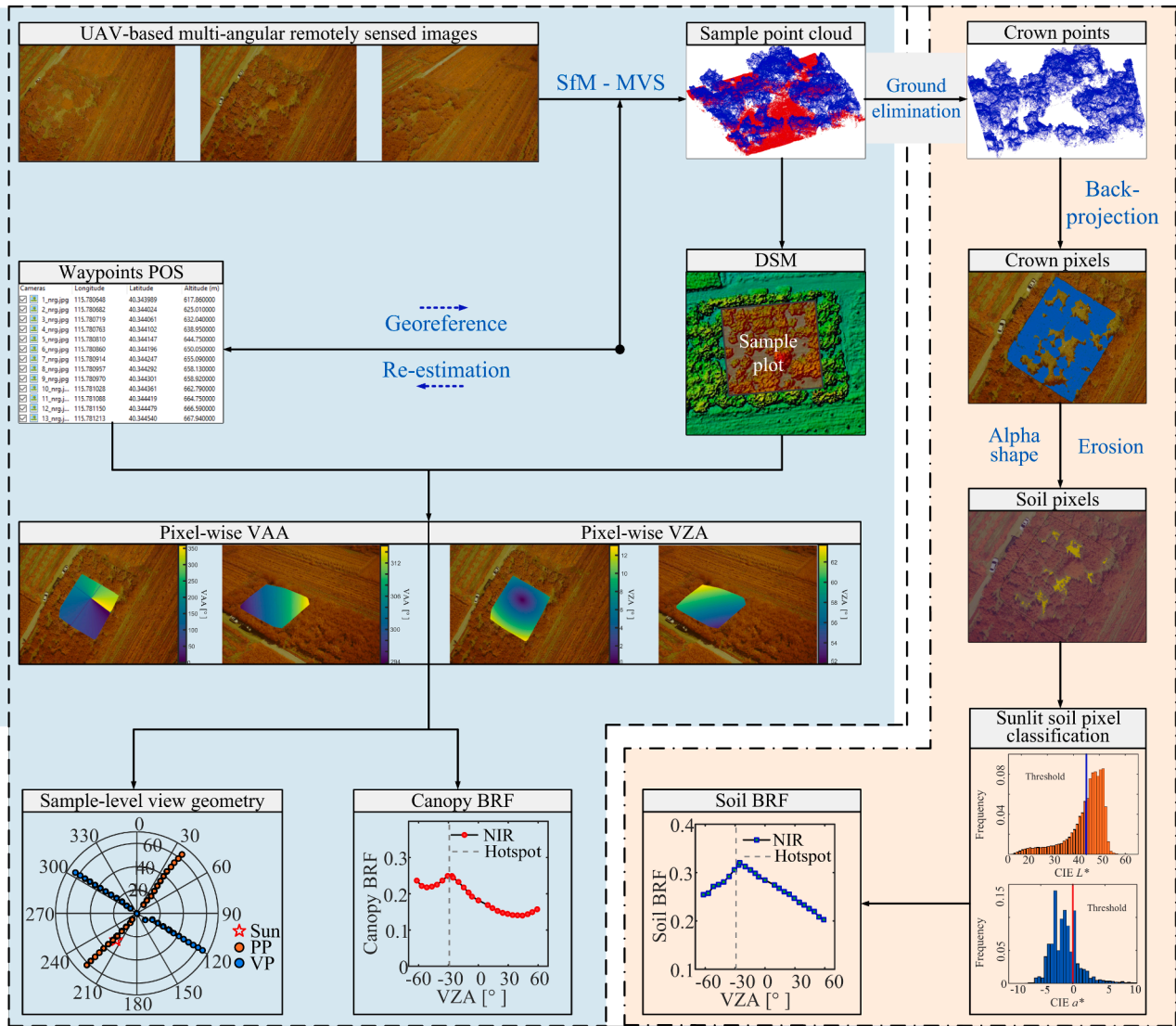
Fig. 6. The workflow for deriving the background soil BRF and canopy BRF from UAV-based multiangular images. Abbreviations: structure-from-motion multi-view stereo (SfM-MVS), digital surface model (DSM), view azimuth angle (VAA), view zenith angle (VZA), near-infrared (NIR), principal plane (PP), and vertical plane (VP).

(2) Geolocation of image pixels

The DSM of the orchard plot area (Fig. 6, Sample point cloud) was projected to each original UAV-based image based on collinearity restrictions using a custom-developed Python script. In other words, the 3D coordinates of DSM were transformed into 2D pixel coordinates of an image using the camera's interior and exterior orientation elements that were automatically calculated by PhotoScan. As a result, the corresponding image pixels were geolocated according to the projected 3D coordinates. The plot area was then extracted from the image acquired at each view angle using a 2D convex hull of the projected pixels. However, because the spatial resolution of the DSM is coarser than the original UAV image and the projected pixels in each image were not spatially continuous, a bilinear interpolation process was applied to derive the geolocations of all pixels within the plot area of each image. Note that the multiangular images had different 2D pixel coordinates and zone shapes for the plot area depending on their view geometries, the number of pixels of the plot area in each image is different.

(3) Calculation of pixel-wise view geometry

Based on the trigonometric relationship between the position of the

camera and ground point, view geometry information, including the view zenith angle (VZA: θ) and view azimuth angle (VAA: φ), was calculated with Eq. 2–3 for each pixel (Fig. 6, Pixel-wise VAA and Pixel-wise VZA):

$$\varphi_p = \begin{cases} \arctan\left(\dfrac{x_c - x_p}{y_c - y_p}\right), & x_c - x_p > 0, y_c - y_p > 0 \\[2mm] \pi + \arctan\left(\dfrac{x_c - x_p}{y_c - y_p}\right), & x_c - x_p < 0, y_c - y_p < 0 \\[2mm] \pi + \arctan\left(\dfrac{x_c - x_p}{y_c - y_p}\right), & x_c - x_p > 0, y_c - y_p < 0 \\[2mm] 2\pi + \arctan\left(\dfrac{x_c - x_p}{y_c - y_p}\right), & x_c - x_p < 0, y_c - y_p > 0 \end{cases} \tag{2}$$

$$\theta_p = \frac{\pi}{2} - \arctan\left(\frac{z_c - z_p}{\sqrt{\left(x_c - x_p\right)^2 + \left(y_c - y_p\right)^2}}\right) \tag{3}$$

where subscripts p and c refer to the original pixel associated with the

ground point and camera, respectively; x and y are X and Y coordinates of the UTM system respectively; z is the altitude.

(4) Soil BRF extraction

The plantation background consists of sunlit and shaded soil components under direct solar illumination. The extraction of soil BRF was implemented based on the sunlit soil component. We extracted the soil pixels based on canopy point cloud and then separately classified the soil pixels into the sunlit and shaded soil pixels using an image segmentation method. The canopy points were firstly identified from the 3D point cloud (Fig. 6, Crown point cloud) using a ground filter called a cloth-simulation filter (CSF) (Zhang et al., 2016) and a height segmentation. The canopy points were then back-projected to the original UAV images to mask the canopy and expose the soil (Fig. 6, Crown pixels). As the 3D canopy points sometimes do not cover all canopy pixels, an additional alpha-shaped polygon was computed to maximize the delineation of canopy pixels and to export soil pixels. Furthermore, a morphological image erosion method was applied to ensure that the selected soil pixels were positioned away from canopy pixels to alleviate multiple scattering effects (Fig. 6, Soil pixels). Next, the extracted soil pixels were classified into sunlit and shaded components through threshold-based segmentations in the CIE $L^*a^*b^*$ color space where the threshold was automatically determined (Fig. 6, histograms in Sunlit soil pixel classification). The green fallen leaves and grass that might occasionally distribute across the ground surface in some cases, were excluded via an image segmentation in the CIE a^* channel (Li et al., 2018; Yan et al., 2019). The CIE L^* channel characterizing brightness feature was used to identify sunlit soil pixels. Finally, the soil BRF of a plot was computed as the average BRF of sunlit soil pixels in the plot (Fig. 6, Soil BRF). Given that the background soil was spatially homogeneous within such a small plot, the BRF of the selected soil patches can represent the background soil in a plot. Apart from the soil BRF, the canopy BRF of a sample plot was calculated by aggregating the BRF of all the pixels within the plot (Fig. 6, Canopy BRF). The plot-level VZA and VAA were set as the mean value and median value of the pixel angles within the plot, respectively.

3.1.2. Soil BRF modeling by SOILSPECT model

To obtain soil anisotropic characteristics over full hemispherical space, the SOILSPECT model (Jacquemoud et al., 1992), a parameterized radiative transfer model derived from the Hapke model (Hapke, 1981), was used to produce the modeled soil BRF because it can model soil anisotropy with prominent accuracy for varying measurement conditions (R^2 of larger than 0.99 and RMSE of less than 0.02) (Jacquemoud et al., 1992). The six-parameter model includes a single scattering albedo (ω), roughness parameter (h) governing the width of the hotspot, and four phase function coefficients (b, c, b', c'). The reflected radiance (L) in the direction ($\theta_r, 0$) received by the sensor is composed of a single scattering term (L_s) and multiple scattering term (L_m) when the soil medium is illuminated by incoming radiant intensity (J) in direction (θ_i, ϕ) as Eq. (4) shows (Jacquemoud et al., 1992):

$$L = L_s + L_m = \frac{J\omega}{4\pi} \frac{cos\theta_i}{cos\theta_i + cos\theta_r} \{[1 + B(g)]P(g, g') + H(cos\theta_i)H(cos\theta_r) - 1\} \quad (4)$$

where $H(x) = (1 + 2x)/(1 + 2\sqrt{1 - \omega x})$ is an approximation of Chandrasekhar's H-function.

The phase function $P(g, g')$ accounts for both the backward and forward scattering of smooth soils by Eq. (5) where g represents the phase angle (i.e., the zenith angle between the incident angle and reflected angle) and g' refers to the angle between the reflected light direction and specular direction. In the original publication (Jacquemoud et al., 1992), the phase function is approximated by a second-order Legendre polynomial.

$$\begin{cases} P(g, g') = 1 + bcosg + c\frac{3cos^2g - 1}{2} + b'cosg' + c'\frac{3cos^2g' - 1}{2} \\ cosg = cos\theta_i cos\theta_r + sin\theta_i sin\theta_r cos\phi \\ cosg' = cos\theta_i cos\theta_r - sin\theta_i sin\theta_r cos\phi \end{cases} \quad (5)$$

To explain the reflectance properties of rough soil, a simplified hotspot function $B(g)$ is introduced considering phase angle g and roughness parameter h, as shown in Eq. (6):

$$B(g) = \frac{1}{1 + (1/h)\tan(g/2)} \quad (6)$$

In this study, the SOILSPECT model was adjusted with the UAV-derived soil BRF profile of each plot. Due to the prominent anisotropy in the PP, only values observed close to the PP were used for the retrieval of model parameters. The retrieved parameters of SOILSPECT served as the input of the LESS simulation for the uncertainty analysis in the following section.

3.2. Uncertainty analysis of soil BRF based on LESS model

The soil BRF extracted from UAV-based multiangular images was mixed with a soil-canopy multiple scattering signal due to the presence of multiple scattering between canopy foliage elements and sunlit soil in between-crown gaps. We quantified the magnitude of the multiple scattering effects through simulations by using the LESS model. The difference between the actual soil BRF and the soil BRF estimated from the simulated multiangular images of forest scenarios reflected the multiple scattering effects.

Various virtually realistic forest scenarios characterizing different canopy cover levels (i.e., 0.17, 0.30, 0.44, 0.76, and 0.92) were created. A basic birch model (*Betula pendula*) originated from a 3-D realistic tree structure modeling software, OnyxTREE BROADLEAF 7.0 (Onyx Computing, Inc., Cambridge, USA), was used to establish the virtual 3D forest scenarios with a size of 50 m × 50 m. We replicated the basic tree model across each forest scenario by adjusting tree numbers and locations (Li et al., 2020b) where the tree positions were generated based on a Poisson spatial distribution function.

LESS, as a 3D radiative transfer model, can accurately and efficiently simulate spectral reflectance and images of vegetation scenes from the visible to thermal infrared domains (Qi et al., 2017, 2019). The BRF simulated by LESS is consistent with those of other classic models (e.g., the DART model) applying the RAMI exercise under different forest scenarios. The backward path tracing of LESS traces only rays that enter the sensor, making it effective in simulating images. To operate LESS for image simulation, one needs to import a 3D scene file (e.g., forest scenarios), and set the illumination and observation geometry, the optical properties of vegetation components (spectral reflectance or PROSPECT model parameters (Jacquemoud and Baret, 1990)), and the optical properties of background soil (spectral reflectance or SOILSPECT model parameters). In our simulation, the SOILSPECT model parameters were collected from the soil of Plot 2 (Table 1), given that its relatively higher reflectance anisotropy could strengthen the interaction between canopy elements and soil. As Table 3 shows, multiangular images at 850 nm with VZA of ranging from −70° to 70° with an angle interval of 10° in the PP were simulated through the LESS model at five canopy cover levels and four SZAs (i.e., 0°, 20°, 40°, and 60°).

The extraction of the soil BRF from the simulated multiangular images is much easier than that from field-acquired UAV images because the locations of sunlit soil pixels in the simulated image were exactly known from the LESS output. We derived the estimated soil BRF from those sunlit soil pixels positioned away from crown pixels in each directional image using the image morphological erosion technique, minimizing multiple scattering effects (Fig. 7).

Table 3

Inputs of the LESS model for the simulations of multiangular images of virtual forest scenarios under different canopy cover levels and solar zenith angles, in order to analyze the uncertainties of the soil BRF estimate from the multiangular image.

Parameters	Value	Description
Structure		
Tree location	Poisson distribution	3 m minimum between trees
Tree model	3D birch model	OnyxTREE BROADLEAF 7.0
Canopy cover	0.17; 0.30; 0.44; 0.76; 0.92	
Optical property		
Wavelength	850 nm	Field spectral measurements
Leaf reflectance	0.45	
Branch reflectance	0.27	
Soil optical property	SOILSPECT parameters of Plot 2	Anisotropic soil
Illumination		
Solar zenith angle	0°; 20°; 40°; 60°	From nadir to large off-nadir angle
Solar azimuth angle	180°	

Table 4

Inputs of the LESS model for the simulations of canopy BRF under various soil moisture levels, canopy cover levels, and solar zenith angles, in order to assess the soil anisotropy effect on the canopy BRF.

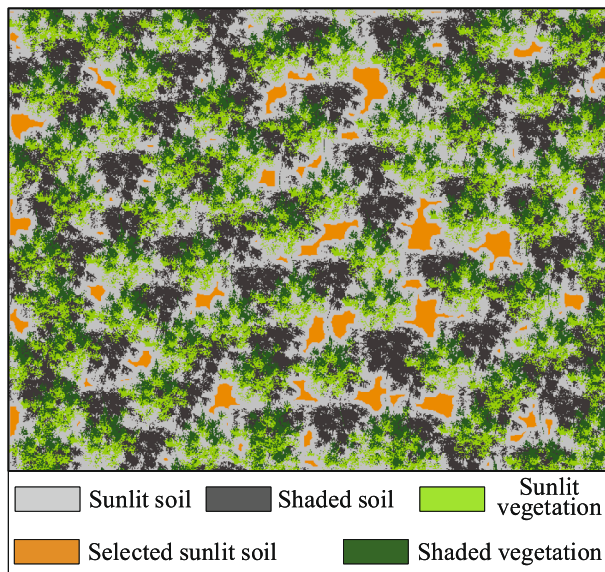| Parameters	Value	Description
Structure		
Tree location	Poisson distribution	3 m minimum between trees
Tree model	3D birch model	OnyxTREE BROADLEAF 7.0
Canopy cover	0.17; 0.30; 0.44; 0.76; 0.92	
Optical property		
Wavelength	851 nm	From reflectance library
Leaf reflectance	0.39	
Branch reflectance	0.26	
Soil moisture level	Dry; slightly moist; very moist	Jacquemoud et al., (1992)
Anisotropic soil	SOILSPECT model predictions	
Lambertian soil	SOILSPECT-predicted nadir BRF	
Illumination		
SZA	0°; 20°; 40°; 60°	From nadir to large off-nadir angle
SAA	180°	

Fig. 7. Classification map of the sunlit and shaded components in a simulated directional image of a forest scenario (canopy cover of 0.30) with a solar zenith angle (SZA) of 20° and view zenith angle (VZA) of 40°. Pixels of the sunlit soil (orange areas) were selected to calculate the soil BRF. (For interpretation of the references to color in this figure legend, the reader is referred to the web version of this article.)

3.3. Evaluation of soil anisotropy effect on canopy BRF based on LESS model

To explicitly understand and quantify discrepancies of the canopy BRF under isotropic background soil and anisotropic soil conditions, the canopy BRF profiles of various virtual forest scenes under different soil moisture content, canopy cover, and SZAs were simulated using Lambertian soil and anisotropic soil, respectively (Table 4). The LESS model was applied to simulate canopy BRF using its forward mode at each user-specified view angle by modeling single and multiple scattering within and between crowns and other components of the radiation field.

In the configuration of simulations, we used the clay soils with three soil moisture content levels (dry soil, slightly moist, and very moist) collected by Jacquemoud et al. (1992) to enrich the simulation, because the soil of the experimental plots in this study was dry (Table 1). The selection of clay soil is reasonable since it is relatively common in

plantation regions. For the anisotropic soil, we obtained the SOILSPECT model parameters of the clay soil (Jacquemoud et al., 1992). For the Lambertian soil, the soil reflectance was set as the SOILSPECT-predicted nadir BRF of the anisotropic soil. This treatment is acceptable because soil reflectance, as the input of the radiative transfer model, is generally measured in the nadir direction (Fang and Liang, 2003). Next, various 3D forest scenarios were created following the procedure described in Section 3.2. The canopy BRFs were simulated with the VZAs from −70° to 70° with an interval of 2° in the PP. Table 4 details the basic structures, the optical properties of scene components, and illumination geometry.

4. Results

4.1. Comparison of soil BRF obtained from UAV and ground observations

As Fig. 8 shows, the UAV-measured soil BRF profiles show good agreement with those measured using a ground multiangular observation system with an RMSE of less than 0.02 in the PP for all plots. Note that the ground-based BRF values were linearly interpolated to calculate the accuracy metrics due to the inconsistent numbers of UAV- and ground-based observations. However, the maximum BRF value associated with the hotspot direction shows slight discrepancies between UAV and ground measurements. Our rough calculation of the view angle of ground observations might explain this problem. The ground-measured BRF profiles showed small jump points due to slight heterogeneity within the observation region. Comparatively, the UAV-measured BRF distribution was more consistent along with the PP. Fig. 8 also shows the fitted soil BRF profiles based on UAV measurements using the SOIL-SPECT model for all plots. The fitted profiles are in line with the measured profiles with R^2 values of larger than 0.92, allowing the accurate characterization of the soil anisotropy by a soil BRDF model, hence providing the input of LESS simulation for the uncertainty analysis in Section 3.3.

The soil BRF at a larger SZA over the plantation background shows a more pronounced bell shape (except Fig. 8d) and lower BRF values in the PP. The BRF values quickly decrease when they shift from the hot-spot direction to other directions. The slow decrease in the BRF at VZAs of larger than 30° might have been caused by a few grasses growing on the ground surface (Fig. 8d). As soil moisture content is different for the three plots, the soil BRF profiles characterize different exact values. Under a similar SZA, dryer soil usually shows pronounced reflectance
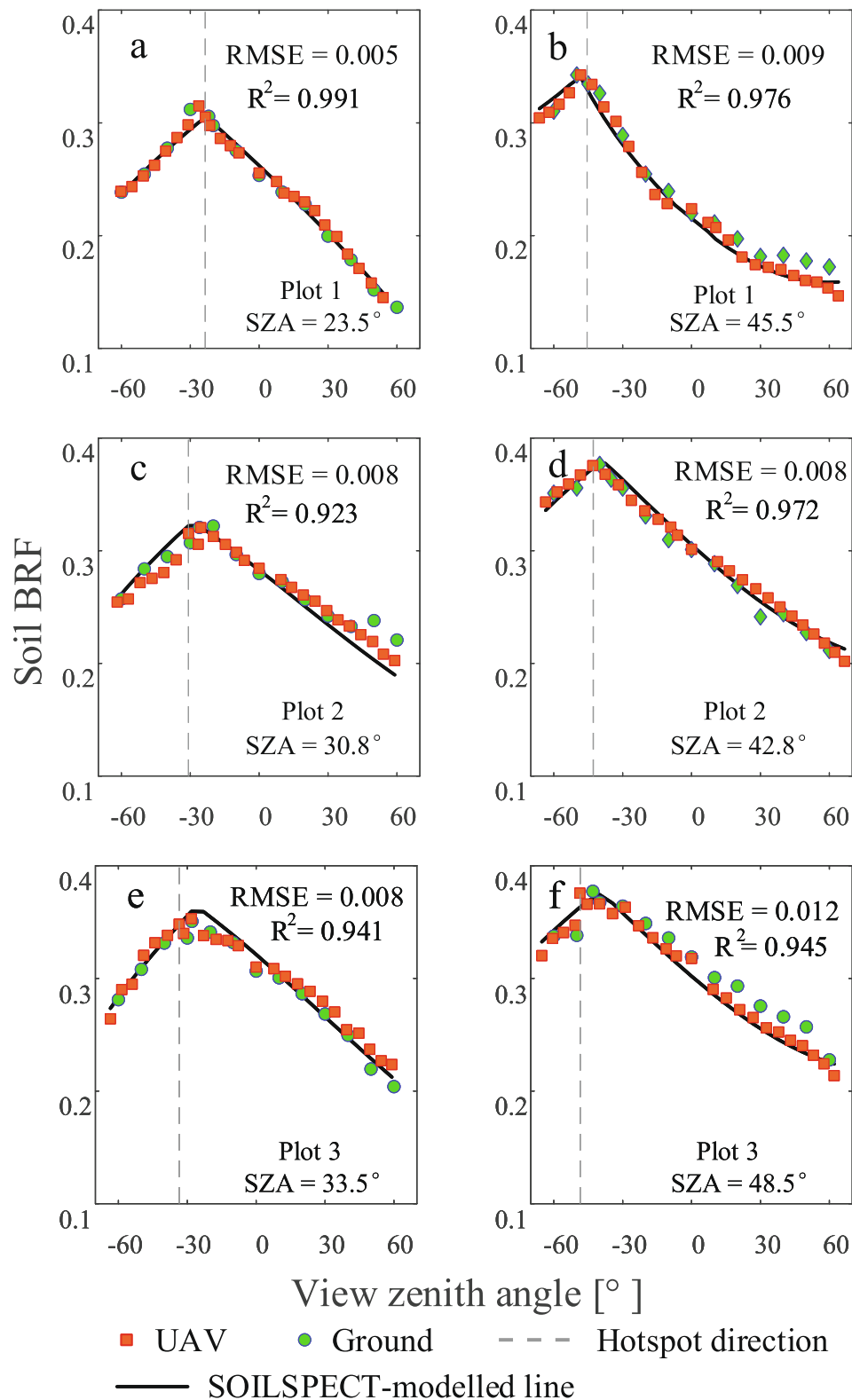
Fig. 8. Soil BRF profiles of Plot 1 (a, b), Plot 2 (c, d), and Plot 3 (e, f) at different sun geometries in the principal plane (PP) at 850 nm. The soil BRF profiles are measured by a ground-based observation system and a UAV. The RMSE values were calculated by using the UAV-measured values and the interpolated ground-measured values. The R^2 values were calculated using the SOILSPECT-fitted and UAV-measured soil BRF.

anisotropy (Tian and Philpot, 2018).

The UAV-based multiangular images also enable the extraction of canopy BRF. As Fig. 9 illustrates, the canopy BRF profiles of all observations taken in the PP in the NIR band are asymmetrical and exhibit a prominent bowl shape, i.e., pronounced anisotropy characteristics. It is noticed that the

canopy BRF values at VZAs of larger than 45° on the forward scattering side were removed for Plot 1 (Fig. 9b), mainly because the radiant flux of the sample plot was blocked by the neighboring tall trees outside the plot. High and low reflectance are distributed in the backscattering (negative VZA) and forward scattering (positive VZA) directions, respectively. The darkest
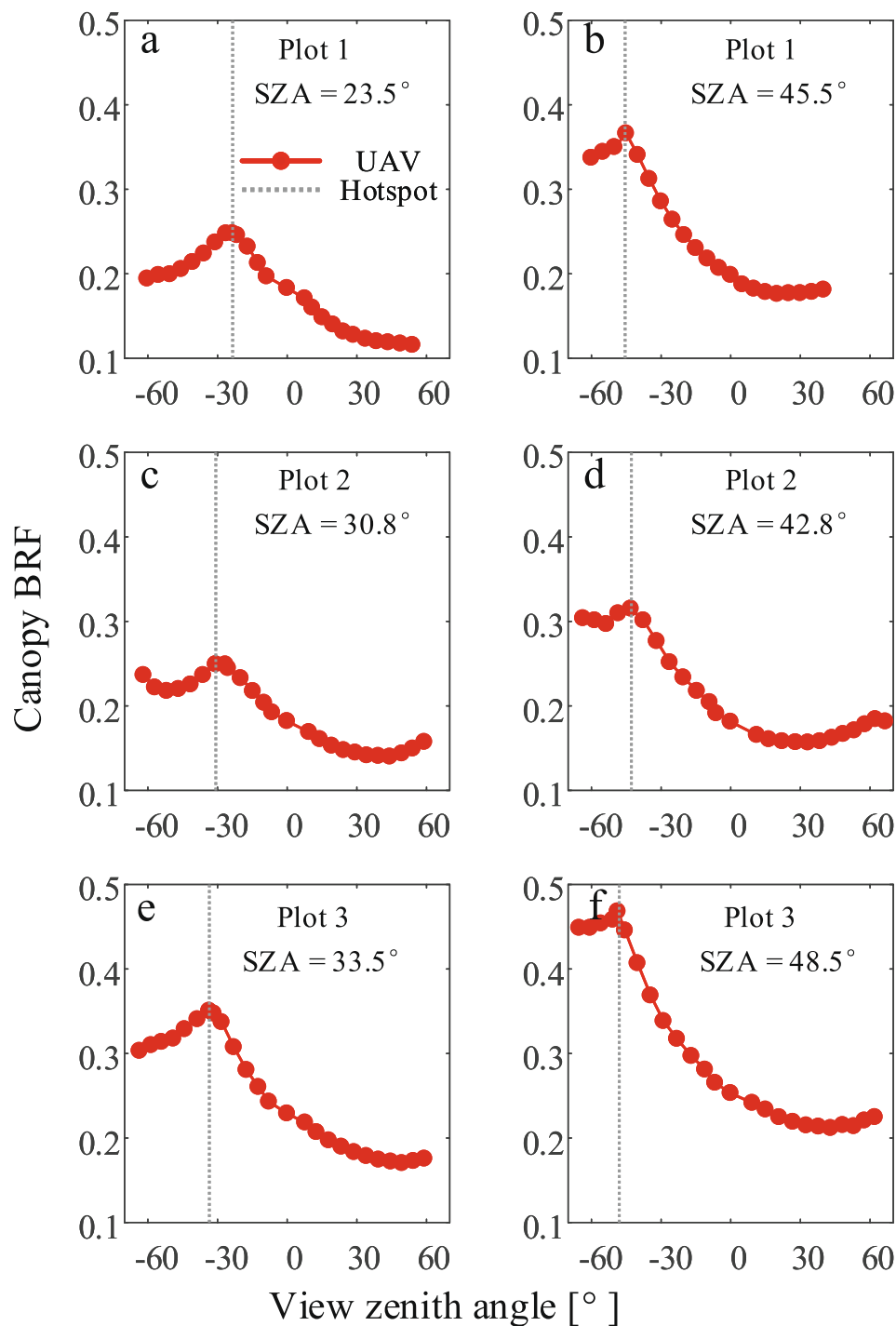
Fig. 9. Canopy BRF of Plot 1 (a, b), Plot 2 (c, d), and Plot 3 (e, f) at different sun geometries in the principal plane (PP) at 850 nm. The view zenith angle in the forward scattering direction of the PP is positive, whereas that in the backward scattering direction of the PP is negative.

region appears over a small VZA on the forward scattering side. The canopy BRF reaches a maximum in the hotspot position and shows no decrease from the nadir direction to the hotspot direction. The canopy BRF at a larger SZA shows a more pronounced bowl shape and increases in BRF values in the PP (Fig. 9a, b; Fig. 9c, d; Fig. 8e, f), especially for the back-scattering direction, since the fraction of sunlit crowns and multiple scattering increase. Under similar SZAs (Fig. 9a, c, and e; Fig. 9b, d, and f), the magnitude of the canopy BRF shows differences among three different 3D structures (i.e., three orchard sample plots) supported by the extensive description of canopy structures, tree species composition and density and optical properties of leaves and soil. This implies that canopy anisotropic characteristics contain

canopy biophysical and biochemical information. The canopy BRF in the hotspot region were apparently not as sharp as the predictions by some canopy BRDF models (Jiao et al., 2016). This can be explained by the aggregation process of the radiant flux over a solid angle of approximately 0.1 sr (FOV of approximately 20°), leading to the concealing of true BRDF features.

4.2. Quantification of UAV-measured soil BRF uncertainty

Fig. 10 compares the soil BRF extracted from simulated images and those of bare soil (i.e., CC = 0) for a range of VZAs, SZAs, and CC levels.
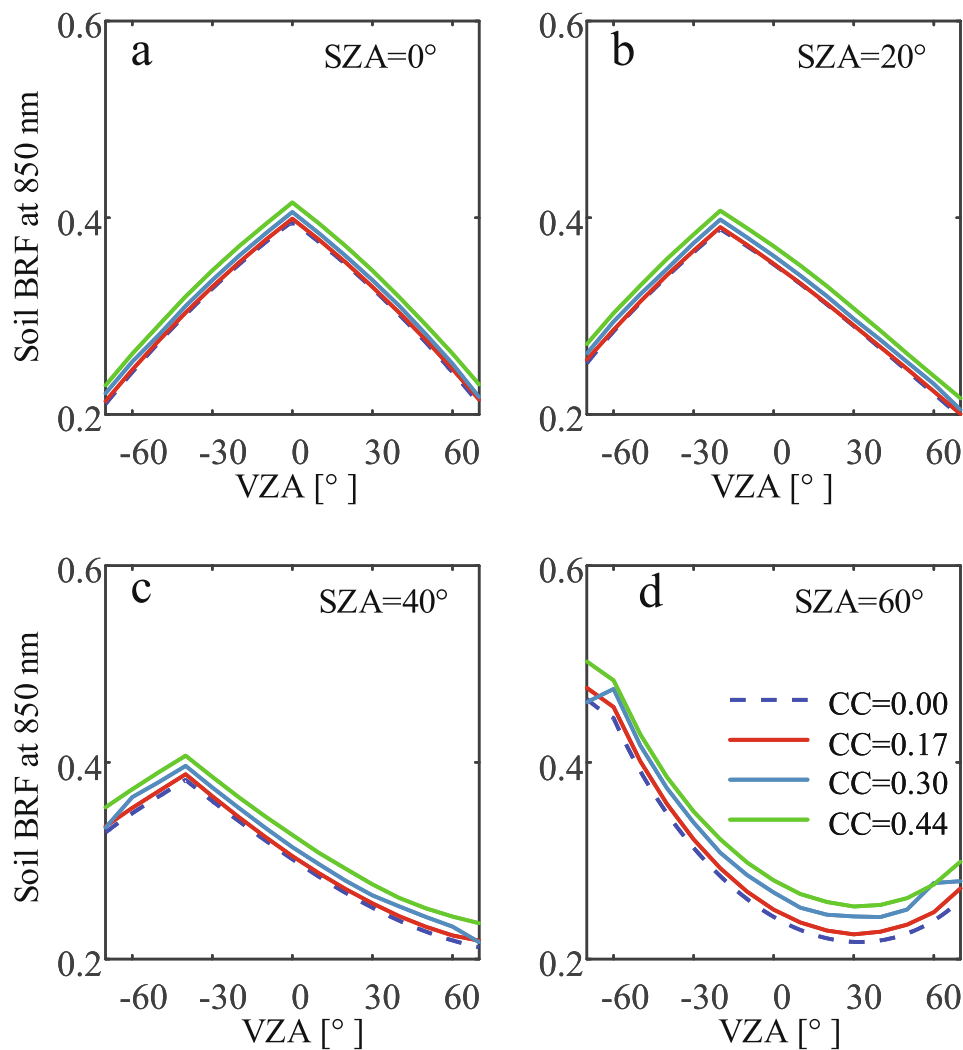
Fig. 10. Comparisons between the soil BRF extracted from simulated images of multiple virtual forest scenarios and that of bare soil for the bare soil scene across a range of view zenith angles (VZAs), solar zenith angles (SZAs), and canopy cover (CC) levels.

Although the LESS simulations for the multiple scattering effect analysis were conducted for all CC levels from 0.17 to 0.92, there is only a small obviously visible sunlit soil component in the simulated directional images for CC of 0.76 and 0.92; thus, no soil BRF values were derived for these two CC levels. As Fig. 10 explains, the difference between the soil BRF of bare soil and that of extracted soil reflects the contribution of multiple scattering effects between foliage elements and background soil. A larger difference indicates a greater contribution to the extracted soil BRF. With a fixed SZA, the multiple scattering effects increase with increasing CC. With fixed CC, the rise of the SZA drives an increase in the multiple scattering effects. Nevertheless, only a small difference (approximately 0.03) between the extracted soil BRF and the true values was found at 850 nm. Specifically, the maximum contribution of multiple scattering to the soil BRF on the backward scattering side is less than 5% for a VZA of 0°, an SZA of 60°, and a CC of 0.44 in the PP, which is acceptable given the 5% quality objective for BRF observation (Widlowski et al., 2014). The results suggest that the soil BRF extracted from UAV-based multiangular images is close to the true soil BRF in the NIR band.

4.3. Difference of simulated canopy BRF under anisotropic soil and Lambertian soil

Simulations of canopy BRF with anisotropic soil are here referred to, for the sake of simplicity, as SAS and those with Lambertian soil are

referred to as SLS. To illustrate noticeable differences between the SAS and SLS, only simulations conducted on dry background soil are shown among different soil moisture content levels in this section (Fig. 11) whereas those under slight moist and very moist soil conditions are provided in the supplementary file (Figs. 12, 13). The simulated canopy BRF profiles with anisotropic soil and Lambertian soil backgrounds under a range of canopy cover levels and SZAs at 850 nm are compared in Fig. 11. Overall, there is a large deviation of canopy BRF values in magnitude and shape between the SAS and SLS when low canopy cover and large SZA values occur, verifying that the reflectance from background soil distorts the signal of the whole canopy. The canopy BRF with SLS shows weaker anisotropy than that of the SAS over the VZA range.

For a given canopy cover (see columns in Fig. 11), the soil anisotropic characteristics become more pronounced in the canopy BRF with an increase in the SZA, especially in back-scattering directions. A larger SZA generally creates an increased bias for the SLS BRF. More precisely, the canopy BRF of the SLS is generally larger than that of the SAS under the smaller SZA, whereas the relationship becomes inverse for a larger SZA. The difference between the SLS BRF and SAS BRF usually increases when the VZA increases, especially for large off-nadir angles. Outside the hotspot region, the difference decreases with the SZA due to the decreasing contribution of the sunlit soil fraction. In addition, the difference varies with the SZA at a given VZA, e.g., the difference in nadir directions is not constant for the four SZAs. This is the case because the
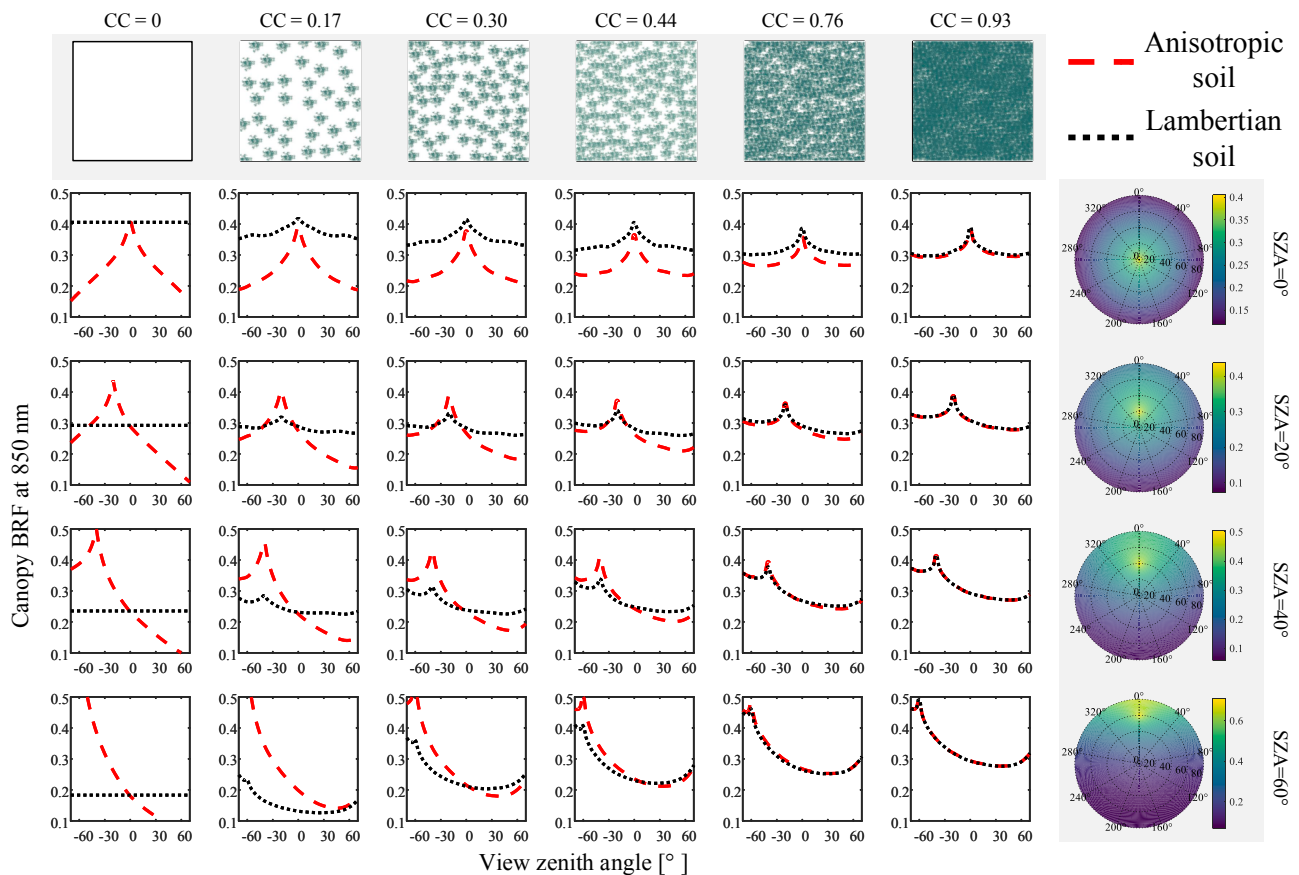
Fig. 11. Comparison of the simulated canopy BRF with anisotropic soil and that with Lambertian soil under different canopy cover (CC) levels and solar zenith angles (SZAs) at 850 nm in dry background soil scenarios. The top row displays five cases of CC levels. The rightmost column exhibits anisotropic characteristics of bare soil at four SZAs.

Lambertian soil reflectance was set as the nadir reflectance of aniso-tropic soil.

For a given SZA (see rows in Fig. 11), the background soil gradually becomes invisible as the canopy cover increases. The difference in the canopy BRF of the SAS and SLS decreases when the canopy cover increases, implying that the BRF is clearly driven by variation in canopy cover. The BRF shape is related to the direction canopy fraction as a function of the VZA and canopy cover. The difference varies with the VZA because directional canopy cover gradually increases when VZA increases. The lesser canopy cover results in a stronger soil effect on canopy anisotropic characteristics since the soil component occupies a larger fraction in the FOV. For low canopy cover levels (e.g., canopy cover of less than 0.5), the absolute error can reach up to 0.3 in the hot-spot direction (Fig. 11 rows 3, 4 and columns 2, 3 of curve plots). This result confirms that the influence of soil anisotropy depends on CC and that less canopy cover will strengthen these effects. For high canopy cover levels (e.g., canopy cover of greater than 0.5), the deviation of the canopy BRF for the SLS approaches zero. The simulations overall demonstrate that the use of soil anisotropy can reduce uncertainties of open radiative transfer simulations.

5. Discussion

5.1. Feasibility of soil BRF extraction from UAV data

The proposed photogrammetry-based image processing algorithm for the derivation of soil BRF was evaluated under multiple illumination and plantation conditions. As the NIR band is particularly important in biophysical variable retrievals (Verrelst et al., 2019), our analysis and results are mainly associated with the NIR band (centered at the 850 nm). The observed consistency between the ground- and UAV-measured soil BRF highlights the potential for UAV multiangular images to accurately characterize forest background optical properties (Fig. 8). Our uncertainty analysis of multiple scattering effects demonstrates the effectiveness of UAV multiangular observations of forest background. The largest bias value of 0.03 recorded at 850 nm confirms that multiple scattering between crowns and soil can be neglected (Fig. 10). For the visible domain, multiple scattering is less pronounced than that in the NIR domain (Shabanov et al., 2000), which implies an even better characterization of soil anisotropy in the visible domain.

The acquisition of UAV-based multiangular images technically provides the possibility for the characterization of reflectance anisotropy. The goniometric pattern of multiangular observations makes the pixel resolutions of the observed plot almost the same for all the directions, offering the geometrical features of image matching in a certain scale which strengthens the capacity of image matching and hence improves the quality of 3D point cloud and the georeferencing accuracy. This allows the calculation of pixelwise view geometry, overcoming the limitations of sensor pointing accuracy. The aerial campaign was conducted on a calm and cloudless day. In such environmental conditions, the canopy elements are generally motionless, i.e., quite small movements relative to the demand of image matching, further enabling accurate image matching among overlapped images. Under clear sky conditions, given that most of the incident flux comes from the sun direction, the

BRF in the visible and near-infrared domains is considered to be well approximated by the hemispherical-directional reflectance factor (HDRF) (Kuusk et al., 2014) although field measurements generally obtain HDRF (both solar directional irradiance and sky diffuse irradiance are present) rather than BRF (Schaepman-Strub et al., 2006). The multiangular measurements in this study are therefore considered as BRF due to the cloud-free conditions. In addition, our 10-minute-long flight minimizes the effect of the variation of sun geometry that the sun moved less than 3° both in zenith and azimuth. With such a small sun movement, the variation of sun geometry might have underestimate BRF at hot-spot direction but the influence on BRF at the other view angles is marginal (Koukal et al., 2014; Roosjen et al., 2016). Moreover, the pixel aggregation at hotspot direction within a FOV can largely alleviate the contribution of sun geometry variation.

The proposed processing technique ensures the accurate characterization of background soil anisotropy. In the procedure, the plantation plot pixels as the region of interest (ROI) were automatically extracted from each directional image, yielding the identical extracted area but different FOVs among multiangular images. The fixed-ROI observation pattern minimizes the interference from the adjacent plants outside of the sample plot, i.e., weakening the scale problem. As Section 3.1.2 described, the soil BRF is derived based on the sunlit soil pixels which can be extracted as long as they are visible in the image. The extracted soil BRF is insensitive to the number of soil pixels and mostly relies on the soil inherent optical properties.

The soil BRF results achieved in this study are reproducible and consistent, but potential biases remain. As the soil reflectance was extracted from large sun-flecks or clear-cuts where tree crowns were almost missing, the measured soil BRF might have errors. These preferred areas are usually under higher levels of sun illumination during the day and thus have drier surfaces, which might differ from the soil areas beneath crowns and in shaded areas. Nevertheless, this bias is less important because sunlit soil dominates the contribution of the reflected signal. Additionally, while soil heterogeneity can introduce bias, it was found to be very slight in our study.

5.2. Influence of soil anisotropy on canopy BRDF simulation

Our investigation based on simulations provides a quantification of soil anisotropy influence on canopy BRF based on canopy structure, sun geometry, and soil moisture conditions (Fig. 11). When canopy cover exceeds 0.5, the influence of soil anisotropy is quite small under any SZA and soil moisture content conditions. Our results are consistent with these previously reported studies that the soil contribution is small and negligible in dense canopies (Choubey and Choubey 1999; Rautiainen 2005). In the case of canopy cover of less than 0.5, the simulation results show that the influence of soil anisotropy is sensitive to the SZA. A smaller SZA generally induces a greater influence of soil on canopy reflectance for most VZAs (the relative error can exceed 100% when soil is dry, SZA = 0°, canopy cover is 0.30 and VZA = 45° for Lambertian soil assumption). This can be explained by the increasing fraction of sunlit soil and the increasing path length with an increasing SZA (Myneni and Ross, 1991) and demonstrates the importance of considering the SZA for BRF-related applications (Chen et al., 2005). We also explored three soil moisture conditions of rough clay soil. Soil anisotropy is weaker when soil is at a higher soil moisture content level, leading to a lower influence on canopy anisotropy (the relative error reduces to about 50% when soil is very moist, SZA = 0°, canopy cover is 0.30 and VZA = 45° for Lambertian soil assumption). Our simulation results reveal that the Lambertian soil assumption is not effective, especially for canopy cover values of less than 0.5. The anisotropic characteristics of a discrete vegetation canopy are considerably affected by soil anisotropy. The influence of soil anisotropy is pronounced in the NIR band due to the stronger scattering effect. This indicates that soil anisotropy must be considered in the radiative transfer modeling of vegetation canopies, especially for the NIR band. Overall, our comparison of the LESS-

simulated canopy BRF with the assumptions of Lambertian and anisotropic background soil verifies the need for accurate soil anisotropy information for open-canopy radiative modelling.

5.3. Spatial variation of forest background

Bare soil backgrounds are common for artificial vegetation scenes, such as the orchard in this study and the plantation forests in some semiarid regions. However, a few types of natural forests are also with bare soil, e.g., the *Populus Euphratica* forests of arid ecosystem grow in bare sandy soil. As a significant reflectance anisotropy has been observed for the bare clay soil in our orchard plots, the sandy soil backgrounds are expected to show higher anisotropic characteristics than clay soil due to their difference in soil texture, surface roughness, organic matter content, moisture and mineralogical composition (Muller and Décamps, 2001). In addition to these plantations and forests, bare soil always appears in agricultural crops but could have a complicated texture, e.g., the plowed soil (Badura and Bachmann, 2019). In the emerging stage of crops that also characterized open-canopy, the soil anisotropy is expected to largely affect canopy BRF, analogous to the open-canopy forest scenes. We suggest applying the proposed method for the above-mentioned open-canopy scenes to extract soil BRF and then analyze the soil anisotropic characteristics.

However, forest background generally refers to all materials (not just bare soil) below the forest canopy, which might include senescent leaves, grass, shrubs, lichen, moss and their combinations, and even snow in the winter season in temperate and boreal forest regions (Pisek and Chen, 2009). In many open forest ecosystems, the forest background is occupied by understory vegetation, such as miniature forests, and has a more compact yet complex structure and more species variation than the overstory canopy (Li et al., 2020a). Correspondingly, the spectral and directional reflectance properties of understory vegetation may vary considerably (Peltoniemi et al., 2005). As the increased roughness often results in stronger anisotropy, the anisotropic characteristics of the understory vegetation might be more pronounced than those of the soil. The former might have a greater influence on canopy directional reflectance. Therefore, the need for anisotropy characterization of understory vegetation might be even stronger, driving the further applications of the proposed method in this study.

5.4. Potential value of UAV-measured soil BRF

This study demonstrated that recent technological advancements in UAVs, lightweight imaging sensors, and multiangular image processing provide new operational systems for the quantitative remote sensing of plantations. This study proposes a feasible means to extract soil BRF profiles from UAV multiangular images, offering strong insight into the anisotropic characteristics of the background of open-canopy areas. In terms of facilitating measurement, with this simple but effective technique, we need not use a field goniometer to measure the forest background BRDF at the plot level due to its labor- and time-consuming nature. Extensive spectral BRDF databases of forest backgrounds (e.g., understory vegetation, soil, and snow) can be established, necessitating further investigations on forest canopy simulation and the retrieval of canopy variables in consideration of soil anisotropy. UAV-measured soil anisotropic characteristics can also be used to produce angular reflectance spectra of forest canopies when simulating a forest landscape with a particular soil type or similar representation (Kuusk et al., 2004), facilitating radiative transfer modeling and validation (Rautiainen and Heiskanen, 2013). Furthermore, with advances in UAV-related technologies, large-area measurements are expected to be able to quantify both the angular and spatial variability of forest backgrounds, which might be relatively high at the scale of satellite pixels (Rautiainen, 2005). The background anisotropy provided by UAVs, as the input of the retrieval model, could improve the accuracy of the estimation of canopy parameters from remote sensing data.

6. Conclusion

This study offers new insight into the characterization of background soil anisotropy with UAV-based multiangular images in open-canopy plots. We developed a photogrammetry-based image processing technique for efficiently extracting the reflectance anisotropy of background soil from multiangular images. UAV-measured soil BRF profiles were found to be in agreement with the ground-based anisotropy measurements (RMSE of less than 0.012). The uncertainty of the measured soil BRF due to multiple scattering was evaluated, and it was confirmed that the effect is negligible even for the NIR band (i.e., 850 nm). A series of 3D radiative transfer simulations based on Lambertian and anisotropic soil (modeled by the SOILSPECT model) was conducted to explore the need for accurate background soil anisotropy. As a result, the assumption of the Lambertian reflectance of forest backgrounds is insufficient to accurately model the canopy BRF (bias can reach up to 0.3). The simulation results also verify that soil anisotropic characteristics cannot be neglected in open forests with canopy cover levels of less than approximately 0.5. The technique proposed in this work can be valuable for validating and advancing soil-canopy radiative transfer models and for the retrieval of vegetation parameters.

Declaration of Competing Interest

The authors declare that they have no known competing financial interests or personal relationships that could have appeared to influence the work reported in this paper.

Acknowledgments

Appendix A. Supplementary material

Supplementary figures to this article can be found online at https://doi.org/10.1016/j.isprsjprs.2021.05.007.

References

Badura, G., Bachmann, C.M., 2019. Assessing Effects of Azimuthally Oriented Roughness on Directional Reflectance of Sand. IEEE J Sel. Top. Appl. Earth Obs. Remote Sens. 12, 1012–1025. https://doi.org/10.1109/JSTARS.2019.2896592.

Baret, F., Buis, S., 2008. Estimating canopy characteristics from remote sensing observations: Review of methods and associated problems, in: Advances in Land Remote Sensing: System, Modeling, Inversion and Application, pp. 173–201.

Burkart, A., Aasen, H., Alonso, L., Menz, G., Bareth, G., Rascher, U., 2015. Angular dependency of hyperspectral measurements over wheat characterized by a novel UAV based goniometer. Remote Sens. 7, 725–746. https://doi.org/10.3390/rs70100725.

Canisius, F., Chen, J.M., 2007. Retrieving forest background reflectance in a boreal region from Multi-angle Imaging SpectroRadiometer (MISR) data. Remote Sens. Environ. 107, 312–321. https://doi.org/10.1016/j.rse.2006.07.023.

Chen, J.M., Menges, C.H., Leblanc, S.G., 2005. Global mapping of foliage clumping index using multi-angular satellite data. Remote Sens. Environ. 97, 447–457. https://doi.org/10.1016/J.RSE.2005.05.003.

Choubey, V.K., Choubey, R., 1999. Spectral Reflectance, Growth and Chlorophyll Relationships for Rice Crop in a Semi-Arid Region of India. Water Resour. Manag. 13, 73–84. https://doi.org/10.1023/A:1008056400348.

Cierniewski, J., Gdala, T., Karnieli, A., 2004. A hemispherical–directional reflectance model as a tool for understanding image distinctions between cultivated and uncultivated bare surfaces. Remote Sens. Environ. 90, 505–523. https://doi.org/10.1016/J.RSE.2004.01.004.

Combal, B., Baret, F., Weiss, M., Trubuil, A., Macé, D., Pragnère, A., Myneni, R., Knyazikhin, Y., Wang, L., 2003. Retrieval of canopy biophysical variables from bidirectional reflectance: Using prior information to solve the ill-posed inverse problem. Remote Sens. Environ. 84, 1–15. https://doi.org/10.1016/S0034-4257(02)00035-4.

Eriksson, H.M., Eklundh, L., Kuusk, A., Nilson, T., 2006. Impact of understory vegetation on forest canopy reflectance and remotely sensed LAI estimates. Remote Sens. Environ. 103, 408–418. https://doi.org/10.1016/j.rse.2006.04.005.

Fang, H., Liang, S., 2003. Retrieving leaf area index with a neural network method: Simulation and validation. IEEE Trans. Geosci. Remote Sens. 41, 2052–2062. https://doi.org/10.1109/TGRS.2003.813493.

Gao, F., Schaaf, C.B., Strahler, A.H., Jin, Y., Li, X., 2003. Detecting vegetation structure using a kernel-based BRDF model. Remote Sens. Environ. 86, 198–205. https://doi.org/10.1016/S0034-4257(03)00100-7.

Gemmell, F., 2000. Testing the Utility of Multi-angle Spectral Data for Reducing the Effects of Background Spectral Variations in Forest Reflectance Model Inversion. Remote Sens. Environ. 72, 46–63. https://doi.org/10.1016/S0034-4257(99)00091-7.

Hapke, B., 1981. Bidirectional reflectance spectroscopy: 1. Theory. J. Geophys. Res. Solid Earth 86, 3039–3054. https://doi.org/10.1029/JB086iB04p03039.

Huang, H., Chen, M., Liu, Q., Liu, Q., Zhang, Y., Zhao, L., Qin, W., 2009. A realistic structure model for large-scale surface leaving radiance simulation of forest canopy and accuracy assessment. Int. J. Remote Sens. 30, 5421–5439. https://doi.org/10.1080/01431160903130911.

Jacquemoud, S., Baret, F., 1990. PROSPECT: A model of leaf optical properties spectra. Remote Sens. Environ. 34, 75–91. https://doi.org/10.1016/0034-4257(90)90100-Z.

Jacquemoud, S., Baret, F., Hanocq, J.F., 1992. Modeling spectral and bidirectional soil reflectance. Remote Sens. Environ. 41, 123–132. https://doi.org/10.1016/0034-4257(92)90072-R.

Jiao, Z., Schaaf, C.B., Dong, Y., Román, M., Hill, M.J., Chen, J.M., Wang, Z., Zhang, H., Saenz, E., Poudyal, R., Gatebe, C., Bréon, F.M., Li, X., Strahler, A., 2016. A method for improving hotspot directional signatures in BRDF models used for MODIS. Remote Sens. Environ. 186, 135–151. https://doi.org/10.1016/j.rse.2016.08.007.

Kimes, D.S., 1991. Radiative Transfer in Homogeneous and Heterogeneous Vegetation Canopies. In: Photon-Vegetation Interactions. Springer Berlin Heidelberg, Berlin, Heidelberg, pp. 339–388. https://doi.org/10.1007/978-3-642-75389-3_11.

Korhonen, L., Korhonen, K., Rautiainen, M., Stenberg, P., 2006. Estimation of forest canopy cover: a comparison of field measurement techniques. Silva Fenn. 40 https://doi.org/10.14214/sf.315.

Koukal, T., Atzberger, C., Schneider, W., 2014. Evaluation of semi-empirical BRDF models inverted against multi-angle data from a digital airborne frame camera for enhancing forest type classification. Remote Sens. Environ. 151, 27–43. https://doi.org/10.1016/J.RSE.2013.12.014.

Kuusk, A., 2001. A two-layer canopy reflectance model. J. Quant. Spectrosc. Radiat. Transf. 71, 1–9. https://doi.org/10.1016/S0022-4073(01)00007-3.

Kuusk, A., Kuusk, J., Lang, M., 2014. Measured spectral bidirectional reflection properties of three mature hemiboreal forests. Agric. For. Meteorol. 185, 14–19. https://doi.org/10.1016/j.agrformet.2013.10.011.

Kuusk, A., Lang, M., Nilson, T., 2004. Simulation of the reflectance of ground vegetation in sub-boreal forests. Agric. For. Meteorol. 126, 33–46. https://doi.org/10.1016/J.AGRFORMET.2004.05.004.

Kuusk, A., Nilson, T., 2000. A Directional Multispectral Forest Reflectance Model. Remote Sens. Environ. 72, 244–252. https://doi.org/10.1016/S0034-4257(99)00111-X.

Laurent, V.C.E., Verhoef, W., Clevers, J.G.P.W., Schaepman, M.E., 2011. Inversion of a coupled canopy–atmosphere model using multi-angular top-of-atmosphere radiance data: A forest case study. Remote Sens. Environ. 115, 2603–2612. https://doi.org/10.1016/J.RSE.2011.05.016.

Li, L., Chen, J., Mu, X., Li, W., Yan, G., Xie, D., Zhang, W., 2020a. Quantifying Understory and Overstory Vegetation Cover Using UAV-Based RGB Imagery in Forest Plantation. Remote Sens. 2020, Vol. 12, Page 298 12, 298. https://doi.org/10.3390/RS12020298.

Li, L., Mu, X., Macfarlane, C., Song, W., Chen, J., Yan, K., Yan, G., 2018. A half-Gaussian fitting method for estimating fractional vegetation cover of corn crops using unmanned aerial vehicle images. Agric. For. Meteorol. 262, 379–390. https://doi.org/10.1016/J.AGRFORMET.2018.07.028.

Li, L., Mu, X., Soma, M., Wan, P., Qi, J., Hu, R., Zhang, W., Tong, Y., Yan, G., 2020b. An Iterative-Mode Scan Design of Terrestrial Laser Scanning in Forests for Minimizing Occlusion Effects. IEEE Trans. Geosci. Remote Sens. 1–20. https://doi.org/10.1109/tgrs.2020.3018643.

Liang, S., Townshend, J.R.G., 1996. A modified Hapke model for soil bidirectional reflectance. Remote Sens. Environ. 55, 1–10. https://doi.org/10.1016/0034-4257(95)00176-X.

Mu, X., Song, W., Gao, Z., McVicar, T.R., Donohue, R.J., Yan, G., 2018. Fractional vegetation cover estimation by using multi-angle vegetation index. Remote Sens. Environ. 216, 44–56. https://doi.org/10.1016/J.RSE.2018.06.022.

Muller, E., Décamps, H., 2001. Modeling soil moisture–reflectance. Remote Sens. Environ. 76, 173–180. https://doi.org/10.1016/S0034-4257(00)00198-X.

Myneni, R.B., Ross, J., 1991. Photon-Vegetation Interactions: Applications in Optical Remote Sensing and Plant Ecology. Springer, Berlin Heidelberg.

Ni, W., Li, X., 2000. A Coupled Vegetation-Soil Bidirectional Reflectance Model for a Semiarid Landscape. Remote Sens. Environ. 74, 113–124. https://doi.org/10.1016/S0034-4257(00)00127-9.

Peltoniemi, J.I., Kaasalainen, S., Näränen, J., Rautiainen, M., Stenberg, P., Smolander, H., Smolander, S., Voipio, P., 2005. BRDF measurement of understory vegetation in pine forests: Dwarf shrubs, lichen, and moss. Remote Sens. Environ. 94, 343–354. https://doi.org/10.1016/j.rse.2004.10.009.

Pinty, B., Verstraete, M.M., Gobron, N., 1998. The effect of soil anisotropy on the radiance field emerging from vegetation canopies. Geophys. Res. Lett. 25, 797–800. https://doi.org/10.1029/98GL00383.

Pisek, J., Chen, J.M., 2009. Mapping forest background reflectivity over North America with Multi-angle Imaging SpectroRadiometer (MISR) data. Remote Sens. Environ. 113, 2412–2423. https://doi.org/10.1016/J.RSE.2009.07.003.

Pisek, J., Chen, J.M., Miller, J.R., Freemantle, J.R., Peltoniemi, J.I., Simic, A., 2010. Mapping Forest Background Reflectance in a Boreal Region Using Multiangle Compact Airborne Spectrographic Imager Data. IEEE Trans. Geosci. Remote Sens. 48, 499–510. https://doi.org/10.1109/TGRS.2009.2024756.

Qi, J., Xie, D., Guo, D., Yan, G., 2017. A Large-Scale Emulation System for Realistic Three-Dimensional (3-D) Forest Simulation. IEEE J Sel. Top. Appl. Earth Obs. Remote Sens. 10, 4834–4843. https://doi.org/10.1109/JSTARS.2017.2714423.

Qi, J., Xie, D., Yin, T., Yan, G., Gastellu-Etchegorry, J.-P., Li, L., Zhang, W., Mu, X., Norford, L.K., 2019. LESS: LargE-Scale remote sensing data and image simulation framework over heterogeneous 3D scenes. Remote Sens. Environ. 221, 695–706. https://doi.org/10.1016/J.RSE.2018.11.036.

Rautiainen, M., 2005. Retrieval of leaf area index for a coniferous forest by inverting a forest reflectance model. Remote Sens. Environ. 99, 295–303. https://doi.org/10.1016/J.RSE.2005.09.004.

Rautiainen, M., Heiskanen, J., 2013. Seasonal Contribution of Understory Vegetation to the Reflectance of a Boreal Landscape at Different Spatial Scales. IEEE Geosci. Remote Sens. Lett. 10, 923–927. https://doi.org/10.1109/LGRS.2013.2247560.

Roosjen, P., Suomalainen, J., Bartholomeus, H., Clevers, J., 2016. Hyperspectral Reflectance Anisotropy Measurements Using a Pushbroom Spectrometer on an Unmanned Aerial Vehicle—Results for Barley, Winter Wheat, and Potato. Remote Sens. 8, 909. https://doi.org/10.3390/rs8110909.

Roosjen, P., Suomalainen, J., Bartholomeus, H., Kooistra, L., Clevers, J., 2017. Mapping Reflectance Anisotropy of a Potato Canopy Using Aerial Images Acquired with an Unmanned Aerial Vehicle. Remote Sens. 9, 417. https://doi.org/10.3390/rs9050417.

Roosjen, P.P.J., Brede, B., Suomalainen, J.M., Bartholomeus, H.M., Kooistra, L., Clevers, J.G.P.W., 2018. Improved estimation of leaf area index and leaf chlorophyll content of a potato crop using multi-angle spectral data – potential of unmanned aerial vehicle imagery. Int. J. Appl. Earth Obs. Geoinf. 66, 14–26. https://doi.org/10.1016/j.jag.2017.10.012.

Roujean, J., 1992. A Bidirectional Reflectance Model of the Earth's Surface for the Correction of Remote Sensing Data A model of correction of bidirectional effects is also, J. Geophys. Res.

Sandmeier, S.R., Itten, K.I., 1999. A field goniometer system (FIGOS) for acquisition of hyperspectral BRDF data. IEEE Trans. Geosci. Remote Sens. 37, 978–986. https://doi.org/10.1109/36.752216.

Schaepman-Strub, G., Schaepman, M.E., Painter, T.H., Dangel, S., Martonchik, J.V., 2006. Reflectance quantities in optical remote sensing—definitions and case studies. Remote Sens. Environ. 103, 27–42. https://doi.org/10.1016/J.RSE.2006.03.002.

Schneider-Zapp, K., Cubero-Castan, M., Shi, D., Strecha, C., 2019. A new method to determine multi-angular reflectance factor from lightweight multispectral cameras with sky sensor in a target-less workflow applicable to UAV. Remote Sens. Environ. 229, 60–68. https://doi.org/10.1016/j.rse.2019.04.007.

Schwieder, M., Buddeberg, M., Kowalski, K., Pfoch, K., Bartsch, J., Bach, H., Pickert, J., Hostert, P., 2020. Estimating Grassland Parameters from Sentinel-2: A Model Comparison Study. PFG – J. Photogramm. Remote Sens. Geoinf. Sci. 88, 379–390. https://doi.org/10.1007/s41064-020-00120-1.

Shabanov, N.V., Knyazikhin, Y., Baret, F., Myneni, R.B., 2000. Stochastic Modeling of Radiation Regime in Discontinuous Vegetation Canopies. Remote Sens. Environ. 74, 125–144. https://doi.org/10.1016/S0034-4257(00)00128-0.

Sharma, R.C., Kajiwara, K., Honda, Y., 2013. Estimation of forest canopy structural parameters using kernel-driven bi-directional reflectance model based multi-angular vegetation indices. ISPRS J. Photogramm. Remote Sens. 78, 50–57. https://doi.org/10.1016/j.isprsjprs.2012.12.006.

Tian, J., Philpot, W., 2018. Soil directional (biconical) reflectance in the principal plane with varied illumination angle under dry and saturated conditions. SPIE-Intl. Soc. Opt. Eng., p. 20. https://doi.org/10.1117/12.2324550.

Verhoef, W., 1984. Light scattering by leaf layers with application to canopy reflectance modeling: The SAIL model. Remote Sens. Environ. 16, 125–141. https://doi.org/10.1016/0034-4257(84)90057-9.

Verhoef, W., Bach, H., 2007. Coupled soil–leaf-canopy and atmosphere radiative transfer modeling to simulate hyperspectral multi-angular surface reflectance and TOA radiance data. Remote Sens. Environ. 109, 166–182. https://doi.org/10.1016/J.RSE.2006.12.013.

Verrelst, J., Malenovský, Z., Van der Tol, C., Camps-Valls, G., Gastellu-Etchegorry, J.-P., Lewis, P., North, P., Moreno, J., 2019. Quantifying Vegetation Biophysical Variables from Imaging Spectroscopy Data: A Review on Retrieval Methods. Surv. Geophys. 40, 589–629. https://doi.org/10.1007/s10712-018-9478-y.

Weiss, M., Baret, F., 1999. Evaluation of Canopy Biophysical Variable Retrieval Performances from the Accumulation of Large Swath Satellite Data. Remote Sens. Environ. 70, 293–306. https://doi.org/10.1016/S0034-4257(99)00045-0.

Widlowski, J.-L., Côté, J.-F., Béland, M., 2014. Abstract tree crowns in 3D radiative transfer models: Impact on simulated open-canopy reflectances. Remote Sens. Environ. 142, 155–175. https://doi.org/10.1016/J.RSE.2013.11.016.

Yan, G., Li, L., Coy, A., Mu, X., Chen, S., Xie, D., 2019. ISPRS Journal of Photogrammetry and Remote Sensing Improving the estimation of fractional vegetation cover from UAV RGB imagery by colour unmixing. ISPRS J. Photogramm. Remote Sens. 158, 23–34. https://doi.org/10.1016/j.isprsjprs.2019.09.017.

Yan, G., Ren, H., Hu, R., Yan, K., Zhang, W., 2012. A portable Multi-Angle Observation System. In: International Geoscience and Remote Sensing Symposium (IGARSS). pp. 6916–6919. https://doi.org/10.1109/IGARSS.2012.6352572.

Yan, K., Park, T., Yan, G., Chen, C., Yang, B., Liu, Z., Nemani, R.R., Knyazikhin, Y., Myneni, R.B., 2016. Evaluation of MODIS LAI/FPAR product collection 6. Part 1: Consistency and improvements. Remote Sens. 8, 1–16. https://doi.org/10.3390/rs8050359.

Zarco-Tejada, P.J., Miller, J.R., Noland, T.L., Mohammed, G.H., Sampson, P.H., 2001. Scaling-up and model inversion methods with narrowband optical indices for chlorophyll content estimation in closed forest canopies with hyperspectral data. IEEE Trans. Geosci. Remote Sens. 39, 1491–1507. https://doi.org/10.1109/36.934080.

Zhang, W., Qi, J., Wan, P., Wang, H., Xie, D., Wang, X., Yan, G., Zhang, W., Qi, J., Wan, P., Wang, H., Xie, D., Wang, X., Yan, G., 2016. An easy-to-use airborne LiDAR data filtering method based on cloth simulation. Remote Sens. 8, 501. https://doi.org/10.3390/rs8060501.

Zhang, X., Qiu, F., Zhan, C., Zhang, Q., Li, Z., Wu, Y., Huang, Y., Chen, X., 2020. Acquisitions and applications of forest canopy hyperspectral imageries at hotspot and multiview angle using unmanned aerial vehicle platform. J. Appl. Remote Sens. 14, 1. https://doi.org/10.1117/1.jrs.14.022212.